Ab Initio and Dynamics Study of the $O(^3P) + NH_3$ and $O(^3P) + N_2H_4$ Reactions at Hyperthermal Collision Energies

Diego Troya,* Marianne Mosch, and Kayleigh A. O'Neill

Department of Chemistry, Virginia Tech, 107 Davidson Hall, Blacksburg Virginia 24061-0212

Received: July 29, 2009; Revised Manuscript Received: September 28, 2009

The reactions between ground-state oxygen atoms ($O(^3P)$) and the ammonia (NH_3) and hydrazine (N_2H_4) molecules have been studied using electronic-structure and dynamics calculations. Ab initio calculations have been used to characterize the primary reaction channels accessible at hyperthermal energies. These reaction channels are i) hydrogen abstraction, $O + NH_3(N_2H_4) \rightarrow OH + NH_2(N_2H_3)$, ii) H-elimination $O + NH_3(N_2H_4) \rightarrow H + ONH_2(ON_2H_3)$, and iii) N−N breakage (in the reaction involving hydrazine), $O + N_2H_4 \rightarrow ONH_2 + NH_2$. Hydrogen abstraction is the lowest-barrier process, followed by N−N breakage and H-elimination. Comparison of our highest-accuracy calculations (CCSD(T)/CBS//MP2/aug-cc-pVDZ) with a variety of lower-cost electronic-structure methods shows that the BHandHLYP method, in combination with the 6-31G* basis set, captures remarkably well the essential features of the potential-energy surface of all of the reaction channels investigated in this work. Using directly the BHandHLYP/6-31G* combination, we have propagated quasiclassical trajectories to characterize the dynamics of the $O + NH_3$ and $O + N_2H_4$ reactions at hyperthermal energies. The trajectory calculations reveal that hydrogen abstraction is the dominant reaction channel, with cross sections between a factor of 2 and an order of magnitude larger than those for the H-elimination and N−N breakage channels. The dynamics calculations also indicate that most of the energy is partitioned into products relative translation but significant vibrational excitation of products is possible as well. Analysis of angular distributions and opacity functions suggests that whereas the hydrogen-abstraction reactions proceed through a mechanism with a substantial component of stripping dynamics, H-elimination and N−N breakage are dominated by rebound dynamics.

Introduction

Chemical phenomena in low-Earth orbit (LEO) have been intensely studied in recent time for various reasons. Most importantly, the deleterious effect of the natural constituents of LEO on polymeric materials coating spacecraft was once deemed to be the Achilles' heel of space exploration.[1,2] The most abundant species in LEO is ground-state atomic oxygen ($O(^3P)$);[3] therefore, a significant body of work has investigated the reactions of this radical with various materials, ranging from hydrocarbons to fluorocabons and polyimides.[4,5] A defining characteristic of chemical degradation in LEO is the large energy involved in the collisions of LEO's natural species with the orbiting spacecraft. With typical orbital velocities in excess of 7 km/s, collisions between $O(^3P)$ and the surfaces of orbiting satellites mounted in the direction of travel occur at collision energies of about 4.5 eV. Such hyperthermal collision energies open the possibility of reaction pathways that are not significant under thermal conditions,[6] but which can enhance significantly the chemical degradation of a variety of materials.

A second consequence of the high energies involved in collisions on and around spacecraft in orbit is the generation of internally excited reaction products, whose emissions can be monitored from on-orbit or ground-based detectors. A particularly important source of excited species in that region of space is the collision of engine-exhaust constituents with naturally occurring LEO species.[7] Thruster firings used to maintain orbit and control attitude can release substantial amounts of material into orbit at high velocities. Emission from subsequent chemical reactions of the exhaust species with ambient $O(^3P)$ can therefore be used to garner fundamental understanding of these processes remotely. For instance, very recent work has characterized the optical emission emerging from controlled firings in various space-shuttle flights.[8−10] The near-UV emissions investigated in these recent papers originate from electronically excited species, mostly OH(A). This species is surmised to originate in the reaction of $O(^3P)$ with H_2O, a major combustion product present in engine exhaust. Even though the generation of electronically excited OH typically requires collision energies in excess of 4.5 eV, these energies are accessible during thruster firings in LEO due to the combined effect of high orbital and effluent velocities.

In this article, we investigate the reactions of ammonia and hydrazine with $O(^3P)$ atoms at hyperthermal energies with the goal of understanding the initial steps of degradation of these molecules in LEO. Hydrazine is a common thruster fuel of spacecraft operating in LEO (e.g., the space shuttle), and it is used in auxiliary power units. Its combustion is accompanied by ammonia production. Hyperthermal reactions of unburned hydrazine and ammonia molecules released in thruster firings with the natural constituents of LEO are therefore present in that region of space and can contribute to the emission phenomenology described above. In fact, the recent release of hydrazine following the intercept of a U.S. satellite on February 20, 2008 provided an opportunity to monitor emission of the products of the $O(^3P) + N_2H_4$ reaction in LEO.[11]

Earlier theoretical work on the $O(^3P) + NH_3$ system[12] focused on the calculation of the minimum-energy reaction path and thermal rate constants of the hydrogen-abstraction channel (OH

* To whom correspondence should be addressed. E-mail: troya@vt.edu.

10.1021/jp9072747 CCC: $40.75
Published on Web 11/03/2009

+ NH_2) to better understand the large scatter in the numerous experimental rate determinations.[13] However, characterization of high-energy channels and state-to-state dynamics for that reaction is not available yet. Theoretical work on $O(^3P) + N_2H_4$ is still lacking. At the experimental level, substantial effort has been directed to the determination of the thermal rate constants.[14−16] In addition, study of $O(^3P) + N_2H_4$ collisions at 20 eV showed the production of electronically excited species.[17]

The work presented in this article will be focused on characterizing the energetics and dynamics of the $O(^3P) + NH_3$ and $O(^3P) + N_2H_4$ reactions at a theoretical level. For this purpose, we have used two different but complementary theoretical techniques. First, we use electronic-structure calculations to identify and accurately characterize the dominant reaction pathways in collisions of $O(^3P)$ with NH_3 and N_2H_4. Subsequently, we carry out direct-dynamics calculations of $O(^3P) + NH_3$ and N_2H_4 collisions at energies relevant to those available in a LEO environment to better understand the mechanisms of the various reaction pathways open at those high energies. We put particular emphasis on the partitioning of energy in products, as products internal excitation can lead to remote tracing of these reactions in orbit. In this article, we shall not investigate the generation of electronically excited OH in reactions of hydrazine with $O(^3P)$, which leads to optical emission in the near-UV range. Instead, we shed light on the vibrational excitation and the associated infrared emission of the products of the $O(^3P) + N_2H_4$ and $O(^3P) + NH_3$ chemical reactions occurring on the ground-state potential-energy surface.

The remainder of this article is as follows. First, we present electronic-structure calculations of the primary reaction channels involved in collisions of $O(^3P)$ atoms with NH_3 and N_2H_4 at hyperthermal energies. Then, we describe direct-dynamics calculations of $O + NH_3$ and $O + N_2H_4$ collisions, including an analysis of cross sections, product-energy partitioning, and angular distributions. Finally, we summarize our main findings in the conclusions section.

Electronic-Structure Calculations

We have characterized the main stationary points of the primary channels in the $O(^3P) + NH_3$ and $O(^3P) + N_2H_4$ reactions accessible at collision energies of up to 5 eV using several electronic-structure methods. Both density functional theory (DFT) (B3LYP, BHandHLYP, and BHandH functionals), and ab initio methods (second-order Möller-Plesset perturbation theory, MP2, and coupled-cluster theory with single, double, and perturbative triple excitations, CCSD(T)) have been employed in the calculations. The basis sets used to solve the electronic Schrödinger equation include the split-valence 6-31G* basis set and Dunning's correlation-consistent basis sets augmented with diffuse functions (aug-cc-pVNZ, N = D, T, Q). All of the CCSD(T) energies correspond to dual-level calculations with geometries and harmonic frequencies obtained at the MP2/aug-cc-pVDZ level. The electronic-structure calculations correspond to the ground-state triplet potential-energy surfaces, have used unrestricted wave functions, and have been carried out using the *Gaussian 03* package of programs.[18]

There are two main channels in the $O + NH_3$ reaction: 1) hydrogen abstraction to produce $OH + NH_2$, and 2) H-elimination to produce $H + ONH_2$. In the $O + N_2H_4$ reaction there is a channel in addition to abstraction ($O + N_2H_4 \rightarrow OH + N_2H_3$) and H-elimination ($O + N_2H_4 \rightarrow H + ON_2H_3$) that is possible at the collision energies examined in this work. This reaction pathway leads to the $ONH_2 + NH_2$ products, and it will be referred to as N−N breakage in this article.

TABLE 1: Calculated Reaction Energies (Δ_rH) and Barriers ($\Delta H^{\ddagger}$) of the $O + NH_3$ and $O + N_2H_4$ Hydrogen-Abstraction Reactions[a,b]

reaction	$O + NH_3 \rightarrow OH + NH_2$		$O + N_2H_4 \rightarrow OH + N_2H_3$	
method/basis set	$\Delta H^{\ddagger}$	Δ_rH	$\Delta H^{\ddagger}$	Δ_rH
B3LYP/aug-cc-pVDZ	−0.001	0.031		−1.112
B3LYP/6-31G*	0.002	0.143		−0.961
BHandHLYP/6-31G*	0.493	0.279	0.110	−0.701
BHandH/6-31G*	0.161	0.359	−0.194	−0.751
MP2/aug-cc-pVDZ	0.663	0.307	0.377	−0.705
CCSD(T)/aug-cc-pVDZ[c]	0.499	0.235	0.104	−0.755
CCSD(T)/aug-cc-pVTZ[c]	0.459	0.205	0.074	−0.828
CCSD(T)/aug-cc-pVQZ[c]	0.450	0.186	0.062	−0.871
CCSD(T)/CBS[b]	0.443	0.173	0.054	−0.902

[a] Energies are in electronvolts. Missing values at specific levels of theory indicate that no first-order saddle point could be located at that level. [b] Negative barriers correspond to true (positive) barriers on the classical (i.e., not zero-point corrected) potential-energy surface that result in an energy below reagents after the zero-point correction. [c] CCSD(T) calculations have utilized geometries and harmonic frequencies obtained at the MP2/aug-cc-pVDZ level.

Table 1 shows the zero-point-corrected reaction energies and barriers for the hydrogen-abstraction channel in the $O + NH_3$ and $O + N_2H_4$ reactions. The calculations reveal that the $O + NH_3 \rightarrow OH + NH_2$ reaction is slightly endothermic, in good agreement with experiment ($\Delta_rH = 0.234 \pm 0.065$ eV).[19] Our most accurate results (CCSD(T) extrapolated to the complete basis-set limit (CBS)) are, as expected, within the experimental error bar, and therefore we will use them as a benchmark to calibrate the accuracy of the rest of lower-cost methods probed in this study. Of the various DFT functionals investigated, BHandHLYP, in combination with the 6-31G* basis set, seems superior to both B3LYP and BHandH. MP2 clearly overestimates CCSD(T) results, and does not improve upon BHandHLYP, despite requiring a significantly larger computational expenditure. The overestimation of CCSD(T) energies by MP2 calculations is typical of other hydrogen-abstraction reactions.[20]

Most of the trends in the comparison between electronic-structure methods just described for the $O + NH_3 \rightarrow OH + NH_2$ reaction also apply to the $O + N_2H_4 \rightarrow OH + N_2H_3$ reaction, but the latter reaction is predicted to be markedly exothermic by all methods. The absolute difference between the reaction energies of hydrogen abstraction in the $O + NH_3$ and $O + N_2H_4$ systems is approximately 1 eV, which indicates the notably weaker character of an N−H bond in hydrazine compared to ammonia. This large difference in the reaction energy for hydrogen abstraction in the $O + NH_3$ and $O + N_2H_4$ reactions is in strong contrast with analogous hydrogen abstractions in $O(^3P)$ + alkane reactions. For instance, high-accuracy calculations indicate that the hydrogen-abstraction channel in the $O + C_2H_6$ reaction is only 0.13 eV more exothermic than that in the $O + CH_4$ reaction.[21]

Table 1 also shows the calculated reaction barriers. Geometries of the located saddle points are presented in parts a and b of Figure 1. Using Hammond's postulate,[22] it can be predicted that the more exothermic $O + N_2H_4 \rightarrow OH + N_2H_3$ reaction should occur through a lower-energy transition state than the $O + NH_3 \rightarrow OH + NH_2$ reaction, and the ab initio calculations bear out this expectation. According to CCSD(T) predictions, the hydrogen-abstraction barrier when going from the $O + NH_3$ to the $O + N_2H_4$ reaction decreases by approximately 0.4 eV (∼10 kcal/mol). This is a significant reduction, and it implies that whereas hydrogen abstraction will be relatively slow at room temperature for $O + NH_3$, its rate will be orders of magnitude higher for $O + N_2H_4$. A remarkable feature of the calculations

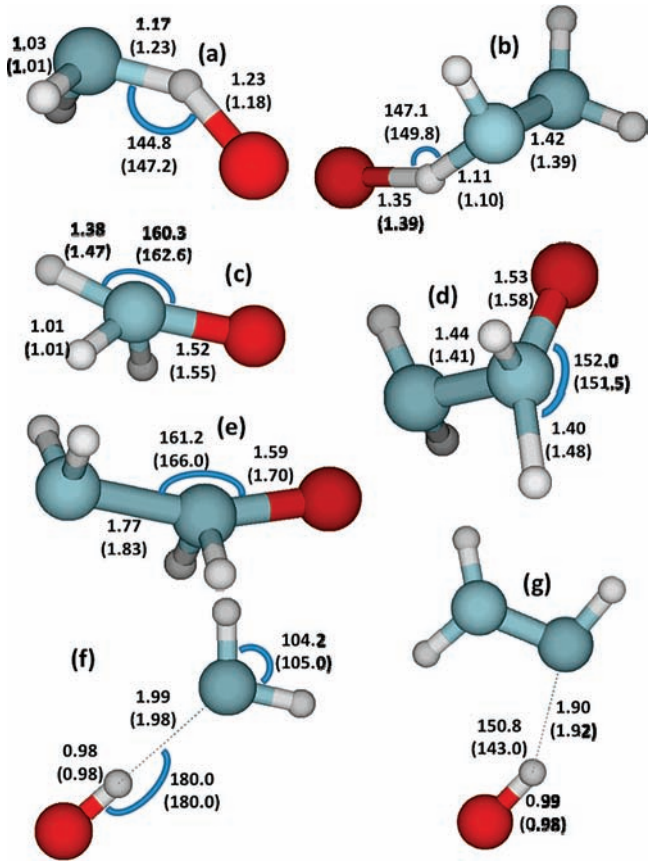

Figure 1. Schematics of various stationary points in the $O(^3P) + NH_3$ and $O(^3P) + N_2H_4$ reactions. (a) Saddle point for the $O(^3P) + NH_3 \rightarrow OH + NH_2$ reaction, (b) saddle point for the $O(^3P) + N_2H_4 \rightarrow OH + N_2H_3$ reaction, (c) saddle point for the $O(^3P) + NH_3 \rightarrow H + ONH_2$ reaction, (d) saddle point for the $O(^3P) + N_2H_4 \rightarrow H + ON_2H_3$, (e) saddle point for the $O(^3P) + N_2H_4 \rightarrow NH_2 + ONH_2$ reaction, (f) minimum in the products' valley of the $O(^3P) + NH_3 \rightarrow OH + NH_2$ reaction, (g) minimum in the products' valley of the $O(^3P) + N_2H_4 \rightarrow OH + N_2H_3$ reaction. The internuclear distances and angles are in Angstroms and degrees respectively and correspond to MP2/aug-cc-pVDZ and BHandHLYP/6-31G* (values in parentheses) results.

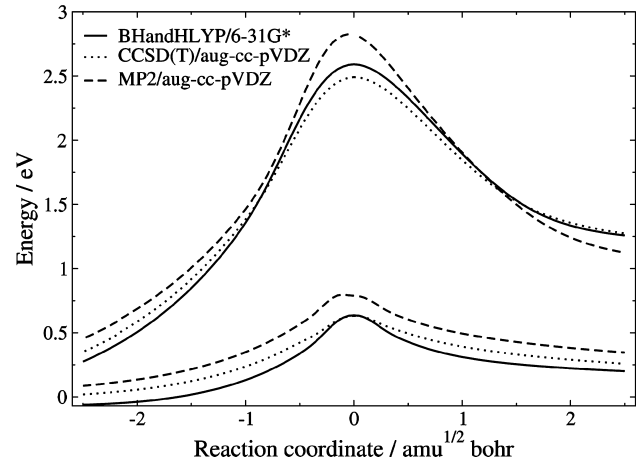

Figure 2. Minimum-energy reaction paths of the hydrogen-abstraction (curves at low energies) and H-elimination (curves at high energies) in the $O(^3P) + NH_3$ reaction. CCSD(T) data correspond to single-point energies on geometries obtained at the MP2/aug-cc-pVDZ level.

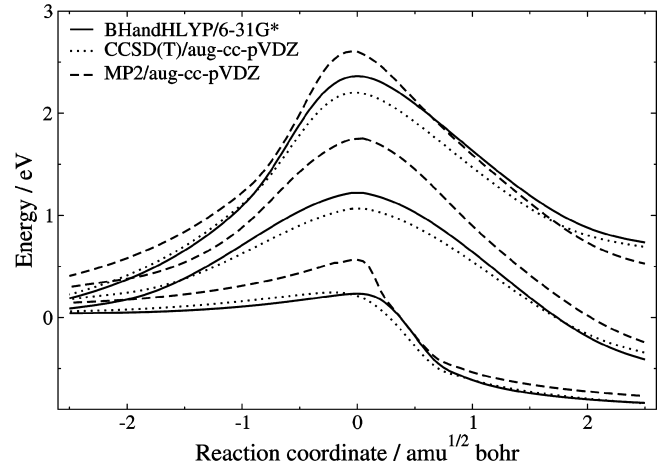

Figure 3. Minimum-energy reaction paths of the hydrogen-abstraction (curves at low energies), H-elimination (curves at high energies), and N−N breakage (curves at intermediate energies) in the $O(^3P) + N_2H_4$ reaction. CCSD(T) data correspond to single-point energies on geometries obtained at the MP2/aug-cc-pVDZ level.

is that the BHandHLYP/6-31G* results reproduce very closely the high-accuracy CCSD(T) data in both the $O + NH_3$ and the $O + N_2H_4$ reactions. The rest of the calculations either significantly overestimate (MP2) or underestimate (B3LYP, BHandH) the CCSD(T) barriers. In fact, for the $O + N_2H_4$, B3LYP calculations were not successful in locating the saddle point for hydrogen abstraction, which is an indication that this method predicts a potential-energy surface that is continuously downhill from reagents to products.

Additional information about the energetics of the hydrogen-abstraction reaction can be obtained from the miminum-energy reaction paths shown in Figure 2 for $O + NH_3$ and in Figure 3 for $O + N_2H_4$. Clearly, BHandHLYP calculations capture the CCSD(T) data more accurately than MP2 calculations, even though the latter are computationally more demanding. Close examination of the points of the hydrogen-abstraction minimum-energy reaction paths closest to the product asymptote indicates the presence of a minimum in the products' valley in both the $O + NH_3$ and the $O + N_2H_4$ reactions. Whereas the minimum-energy reaction paths shown in Figures 2 and 3 do not show these minima directly, the fact that the energy of the points closest to products is below the products asymptotic energy heralds the appearance of these stationary points. Geometry optimizations starting at the last point of the minimum-energy reaction paths of both reactions have located relatively stable $OH-NH_2$ and $OH-N_2H_3$ minima, which emerge primarily due to hydrogen-bonding interactions. The structures of these minima are shown in parts f and g of Figure 1, and their energies relative to the corresponding products asymptotes are listed in Table 2. The data in the table show that DFT calculations predict slightly stronger stabilization of these hydrogen-bonded minima in comparison with MP2 and CCSD(T) calculations. Notwithstanding, the energy differences are small (<2.5 kcal/mol) and will likely play a minor role in dynamics calculations at the collision energies that we have explored in this work, which are at least 20 times larger than the differences between the BHandHLYP and CCSD(T) results.

Table 3 shows the reaction energy and barrier for the $O + NH_3 \rightarrow H + ONH_2$ and $O + N_2H_4 \rightarrow H + ON_2H_3$ H-elimination reactions calculated at the same electronic-structure levels as the hydrogen-abstraction reactions. Schematics of the saddle-point geometries are shown in parts c and d respectively of Figure 1, and minimum-energy reaction paths are in Figures 2 and 3. The electronic-structure calculations indicate that the H-elimination reaction is strongly more endothermic and involves a substantially larger energy barrier than the hydrogen-abstraction reaction. Quantitatively, for both $O + NH_3$ and O

TABLE 2: Calculated Energies of the Potential Minimum in the Products' Valley of the O + NH_3 and O + N_2H_4 Hydrogen Abstraction Reactions[a]

reaction	O + NH_3 → OH + NH_2	O + N_2H_4 → OH + N_2H_3
method/basis set		
B3LYP/6-31G*	0.334	0.500
BHandHLYP/6-31G*	0.349	0.481
MP2/aug-cc-pVDZ	0.272	0.380
CCSD(T)/aug-cc-pVDZ[b]	0.266	0.359
CCSD(T)/aug-cc-pVTZ[b]	0.268	0.368
CCSD(T)/aug-cc-pVQZ[b]	0.266	0.368

[a] Energies are in electronvolts, are not zero-point corrected, and are referred to the corresponding products asymptote. [b] CCSD(T) calculations have utilized geometries at the MP2/aug-cc-pVDZ level.

TABLE 3: Calculated Reaction Energies ($\Delta_r H$) and Barriers ($\Delta H^{\ddagger}$) of the O + NH_3 and O + N_2H_4 H-Elimination Reactions[a]

reaction	O + NH_3 → H + ONH_2		O + N_2H_4 → H + ON_2H_3	
method/basis set	$\Delta H^{\ddagger}$	$\Delta_r H$	$\Delta H^{\ddagger}$	$\Delta_r H$
B3LYP/aug-cc-pVDZ	1.911	0.564	1.616	−0.052
B3LYP/6-31G*	1.842	0.481	1.584	−0.161
BHandHLYP/6-31G*	2.470	1.020	2.201	0.424
BHandH/6-31G*	1.977	0.430	1.672	−0.231
MP2/aug-cc-pVDZ	2.678	0.831	2.387	0.135
CCSD(T)/aug-cc-pVDZ[b]	2.438	1.033	2.128	0.390
CCSD(T)/aug-cc-pVTZ[b]	2.369	0.930	2.077	0.240
CCSD(T)/aug-cc-pVQZ[b]	2.343	0.857	2.058	0.212
CCSD(T)/CBS[b]	2.324	0.803	2.045	0.192

[a] Energies are in electronvolts. [b] CCSD(T) calculations have utilized geometries and harmonic frequencies obtained at the MP2/aug-cc-pVDZ level.

+ N_2H_4, CCSD(T) calculations indicate that H-elimination is over 0.6 eV more endothermic than hydrogen abstraction, and the barrier is almost 2 eV higher. Clearly, the H-elimination reaction requires higher energy than is usually available in thermal or photoinduced experiments and will likely not be observed unless a beam of hyperthermal $O(^3P)$ is produced. In fact, to the best of our knowledge, there is no detailed experimental information to date on the dynamics of the H-elimination channel for either reaction. Recent experiments and calculations on the $O(^3P)$ + HCl reaction have indeed shown that high collision energies open the possibility for H-elimination reaction (to give H + OCl) even if hydrogen abstraction (to give OH + Cl) is the only channel open at low energies.[23]

Comparison of the performance of the various electronic-structure methods examined in this work for the H-elimination channel reveals trends that mirror those described before in the hydrogen-abstraction channel. Whereas B3LYP and MP2 respectively underestimate and overestimate the energies of the stationary points, BHandHLYP, in combination with the 6-31G* basis set, reproduces reasonably well the CCSD(T) calculations. An important conclusion stemming from this result is that the factors controlling the accuracy of the BHandHLYP functional for the hydrogen-abstraction channel (i.e., an adequate balance of exchange and correlation functionals) also govern the accuracy of this method for the H-elimination reaction. This finding suggests the idea that density functionals can be globally accurate for specific multichannel reactions. Examination of the minimum-energy reaction paths for the H-elimination reactions in Figures 2 and 3 shows the faithful reproduction of CCSD(T) data by BHandHLYP calculations. Again, the relatively low-cost BHandHLYP results are a clear improvement over the more demanding MP2 calculations.

TABLE 4: Calculated Reaction Energies ($\Delta_r H$) and Barriers ($\Delta H^{\ddagger}$) of the $O(^3P)$ + N_2H_4 → ONH_2 + NH_2 N−N Breakage Reaction[a]

method/basis set	$\Delta H^{\ddagger}$	$\Delta_r H$
B3LYP/aug-cc-pVDZ	0.732	−1.316
B3LYP/6-31G*	0.557	−1.255
BHandHLYP/6-31G*	1.178	−0.846
BHandH/6-31G*	1.057	−0.945
MP2/aug-cc-pVDZ	1.606	−0.815
CCSD(T)/aug-cc-pVDZ[b]	1.126	−0.854
CCSD(T)/aug-cc-pVTZ[b]	1.078	−0.952
CCSD(T)/aug-cc-pVQZ[b]	1.084	−0.996
CCSD(T)/CBS[b]	1.082	−1.027

[a] Energies are in electronvolts. [b] CCSD(T) calculations have utilized geometries and harmonic frequencies obtained at the MP2/aug-cc-pVDZ level.

Finally, we present in Table 4 the energetics of the stationary points of the $O(^3P)$ + N_2H_4 → ONH_2 + NH_2 N−N breakage reaction. A schematic of the saddle-point geometry is shown in part e of Figure 1, and a depiction of the minimum-energy reaction path can be seen in Figure 3. The calculations show that the N−N breakage channel is slightly more exothermic than hydrogen abstraction, but its barrier is almost 1 eV larger. Still, the N−N breakage reaction has a substantially smaller barrier than the H-elimination reaction and clearly is an energetically allowed reaction channel at collision energies accessible in LEO environment. Examination of the performance of the various electronic-structure methods used in this work reveals trends analogous to those found in the hydrogen-abstraction and H-elimination reactions. An important result is that the BHandHLYP/6-31G* method produces results in close agreement to CCSD(T) data also in this channel. The agreement between these two methods can be evaluated in a larger section of the potential-energy surface via examination of the minimum-energy reaction paths of Figure 3. Clearly, BHandHLYP/6-31G* is the lowest-cost method of those investigated in this work that consistently reproduces higher-accuracy estimates of the energetics of all of the primary channels of the O + NH_3 and O + N_2H_4 reactions. An essential implication of the remarkable performance of BHandHLYP/6-31G* method in describing the energetics of the title reactions is that direct-dynamics calculations employing this method should provide reliable estimates of a variety of reaction-dynamics properties, including cross sections, angular, and product-energy distributions.

Reaction-Dynamics Study

After analyzing the primary reaction pathways in the O + NH_3 and O + N_2H_4 reactions using electronic-structure theory, we now describe the result of quasiclassical trajectory calculations propagated on the BHandHLYP/6-31G* potential-energy surface via direct dynamics. Cross sections, disposal of energy in products, and angular distributions have been computed to provide fundamental understanding of the dynamics of the title reactions at hyperthermal collision energies.

A. Computational Details. Quasiclassical trajectories have been propagated directly at the BHandHLYP/6-31G* level of electronic-structure theory with the *Gaussian 03* suite of programs. Batches of 1000 trajectories have been calculated at 2.25, 3.00, and 4.56 eV collision energy for the O + NH_3 reaction and at 3.00 and 4.56 eV for O + N_2H_4. These collision energies correspond to 7.5, 8.6, 10.7 km/s collision velocities for O + NH_3 and 7.4 and 9.1 km/s for O + N_2H_4, respectively. The trajectories were started at a separation between the O atom

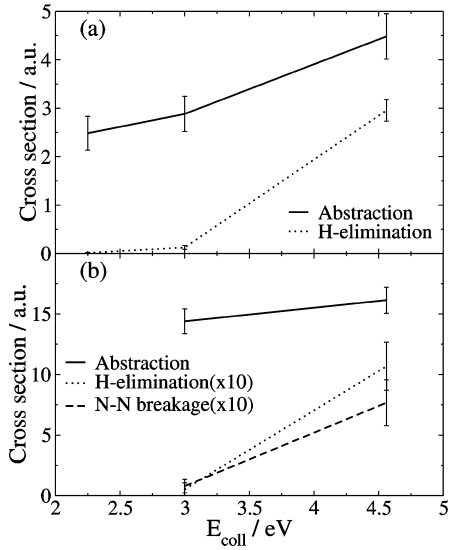

Figure 4. Excitation functions (cross section vs collision energy) for the various reaction pathways of the $O + NH_3$ (a) and $O + N_2H_4$ (b) reactions. The cross sections for H-elimination and N−N breakage in (b) have been multiplied by a factor of 10 for clarity.

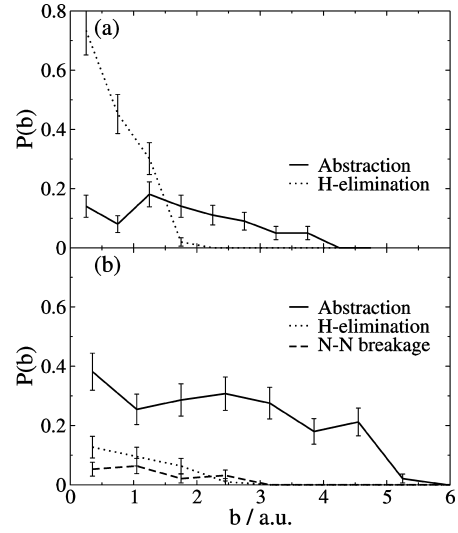

Figure 5. Opacity functions (reaction probability at impact parameter b vs impact parameter) for the various reaction pathways of the $O + NH_3$ (a) and $O + N_2H_4$ (b) reactions at $E_{coll} = 4.56$ eV.

and the center of mass of the molecules of 10 au and were stopped post collision when the separation between the centers of mass of products reached 11 au. The trajectory propagation was conducted via evaluation of first and second derivatives at each integration step. The integration time steps had typical values between 0.35 and 0.50 fs. Overall, 833 113 Hessian calculations were required for the $O + NH_3$ system, and 595 422 for $O+N_2H_4$. Initial coordinates and momenta for the molecules were obtained from zero-point energy motion generated via normal-mode sampling.

B. Reaction Cross Sections. Figure 4 shows the calculated cross sections as a function of collision energy for the $O + NH_3$ and $O + N_2H_4$ reactions. These excitation functions show increasing cross sections with increasing collision energies in the ranges explored in this work. Hydrogen abstraction is the dominant channel in both $O + NH_3$ and $O + N_2H_4$. In $O + NH_3$ (part a of Figure 4), the cross section for H-elimination is almost negligible at the lowest collision energies studied, showing the large barrier for this reaction. However, the H-elimination cross section increases rapidly with collision energy after $E_{coll} = 3.0$ eV and becomes competitive with that for abstraction at the highest collision energy explored (4.56 eV). The result that the cross sections for abstraction and H-elimination are comparable at very high collision energies is interesting because the barriers for these processes are very different (0.493 and 2.470 eV at the BHandHLYP/6-31G* level, respectively). An explanation to this result can be provided by examination of the impact parameters leading to reaction (opacity functions) at $E_{coll} = 4.56$ eV exhibited in part a of Figure 5. The opacity functions for abstraction and H-elimination show that these reactions occur through markedly different reactive impact parameters. Whereas H-elimination is prevalent at small impact parameters and its probability quickly decreases with increasing impact parameters, hydrogen abstraction occurs over a larger range of impact parameters. The opacity functions are consistent with the H-elimination reaction requiring a hard hit between the incoming O atom and the molecule's N atom, which can be anticipated by the transition-state structure shown in part c of Figure 1. On the other hand, the transition state for hydrogen abstraction does not require immediate proximity of the O and N atoms, enabling reaction at larger impact parameters. The remarkably high value of the reaction probability at low-impact parameters for the H-elimination channel implies that many (up to 70%) of the total (reactive + inelastic) trajectories involving a direct interaction between O and N lead to H-elimination at $E_{coll} = 4.56$ eV. This large reaction probability causes the cross section for the H-elimination channel to be comparable to that of the abstraction pathway even if the latter can occur over a significantly larger range of impact parameters.

Part b of Figure 4 shows the cross sections for the abstraction, H-elimination, and N−N breakage channels in the $O + N_2H_4$ reaction. As in the $O + NH_3$ reaction, all of the cross sections increase with collision energy in the examined energy range, with the abstraction channel dominating reactivity. However, several differences become apparent when comparing the excitation functions of the $O + N_2H_4$ and $O + NH_3$ reactions. First, the cross sections for abstraction are between 3 and 5 times larger in the larger reaction. Second, even at the highest energy explored, the abstraction cross section in the $O + N_2H_4$ reaction is more than 1 order of magnitude larger than the cross sections of the H-elimination and N−N breakage channels. On the other hand, the cross sections for abstraction and H-elimination are well within a factor of 2 at $E_{coll} = 4.56$ eV in the $O + NH_3$ reaction. Another difference with the $O + NH_3$ reaction is the appearance of the N−N breakage channel, which has cross sections similar to those of the H-elimination channel. Further insight into some of these trends can be provided by examination of the opacity functions at $E_{coll} = 4.56$ eV in Figure 5. Comparison of the opacity functions for the $O + N_2H_4$ and $O + NH_3$ abstraction reactions indicates that the increase in reactivity of the hydrogen-abstraction channel in the larger reaction has two contributions. First, in $O + N_2H_4$, hydrogen abstraction can take place at longer impact parameters than in $O + NH_3$, which substantially increases reactivity due to the quadratic dependence of the cross section on the maximum reactive impact parameter.[24] Second, the reaction probabilities at the common impact parameters are always larger in the $O + N_2H_4$ reaction. This increase in reactivity seems directly connected to the sharp change in the potential-energy surface for hydrogen abstraction when going from $O + NH_3$ to $O + N_2H_4$. This change can be substantiated by the almost 0.5 eV decrease in the reaction barrier shown in Table 1.

TABLE 5: Average Fractions of Available Energy Partitioned into Various Products' Degrees of Freedom for the $O + NH_3 \rightarrow OH + NH_2$ and $O + N_2H_4 \rightarrow OH + N_2H_3$ Reactions

E_{coll}/eV	$f_{VIB,OH}$	$f_{ROT,OH}$	f_T	$f_{VIB,AMINYL}$	$f_{ROT,AMINYL}$
		$O + NH_3 \rightarrow OH + NH_2$			
2.25	0.02	0.14	0.79	0.00	0.05
3.00	0.03	0.12	0.81	0.00	0.04
4.56	0.02	0.12	0.82	0.01	0.03
		$O + N_2H_4 \rightarrow OH + N_2H_3$			
3.00	0.09	0.08	0.63	0.08	0.12
4.56	0.06	0.09	0.66	0.08	0.11

Regarding the H-elimination and N−N breakage reactions, the opacity functions in part b of Figure 5 show that they occur over the same range of (small) impact parameters. As can be seen in parts d and e of Figure 1, these reactions require a direct interaction or hard hit between the incoming O atom and a N atom, and this is nicely exhibited in the impact parameters of part b of Figure 5. A result of particular interest is that the cross sections for H-elimination and N−N breakage in the $O + N_2H_4$ reaction are within statistical uncertainty of each other. This is noticeable, as the barrier for N−N breakage is approximately 1.3 eV smaller than that for H-elimination and suggests that the cone of acceptance for N−N breakage is substantially narrower than that for H-elimination.

C. Product-Energy Partitioning. We now focus on analyzing how the large amount of available energy in hyperthermal collisions of $O(^3P)$ with NH_3 and N_2H_4 is channeled into products. Table 5 shows the average fractions of available energy partitioned to the various products degrees of freedom in the $O + NH_3 \rightarrow OH + NH_2$ and $O + N_2H_4 \rightarrow OH + N_2H_3$ reactions. Most of the available energy in these hydrogen-abstraction reactions ends up as products relative translation in both systems. In comparison, only a minor fraction of the available energy is channeled into molecular modes. This is particularly true for the $O + NH_3$ reaction, where approximately 80% of the total energy in products corresponds to relative translation and less than 5% ends up in product vibration. In fact, only about 10−25% of the nascent OH molecules result vibrationally excited. Energy partitioning into molecular modes is slightly more important in the $O + N_2H_4$ reaction. For instance, about half of the reactive trajectories produce vibrationally excited OH. In addition, excitation of the aminyl fragment in the $O + N_2H_4$ reaction is much larger than in $O + NH_3$, with approximately 20% of the total energy ending up in the N_2H_3 fragment versus less than 5% appearing in NH_2. These results indicate that the size of the reagent molecule influences the partitioning energy in products, with the larger hydrazine molecule facilitating the coupling of molecular modes to the reaction coordinate. Interestingly, the average fractions do not depend dramatically on collision energy, suggesting that the rate at which the amount of energy goes into the various products' degrees of freedom is commensurate with the increase in the total available energy as the collision energy increases.

Analysis of energy partitioning in the $O + NH_3 \rightarrow H + ONH_2$ and $O + N_2H_4 \rightarrow H + ON_2H_3$ H-elimination reactions shows trends analogous to those just described for the hydrogen-abstraction channel. We describe only the results at $E_{coll} = 4.56$ eV, as the statistical uncertainty of the lower-energy calculations for this channel are relatively large due to the lack of substantial reactive trajectories. For the $O + NH_3$ reaction, 67% of the available energy ends up as product translation, 21% as ONH_2 rotation, and 12% as ONH_2 vibration. For $O + N_2H_4$, 52% of the energy is channeled into products relative translation, with 6% going into ON_2H_3 rotation, and 42% into ON_2H_3 vibration. The conclusion is that much as in the abstraction reaction, the amount of energy disposed in molecular modes is strongly influenced by the reagent molecule. In effect, reactions with hydrazine result in enhanced energy partitioning into the oxyaminyl radical, likely due to the ability to couple a larger number of energy-absorbing modes to the reaction coordinate. The channeling of available energy into ON_2H_3 vibration seems particularly effective, and on average, this molecule receives 40 kcal/mol of vibrational excitation at $E_{coll} = 4.56$ eV.

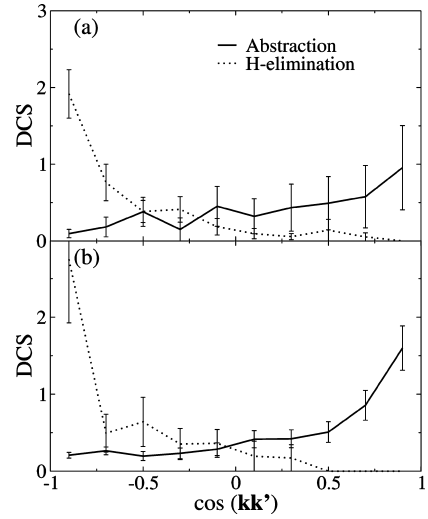

Figure 6. Angular distributions (normalized differential cross sections DCS vs the cosine of the scattering angle) for the abstraction and H-elimination pathways of the $O + NH_3$ (a) and $O + N_2H_4$ (b) reactions at $E_{coll} = 4.56$ eV.

We have also analyzed energy partitioning in the $O + N_2H_4 \rightarrow ONH_2 + NH_2$ reaction at $E_{coll} = 4.56$ eV. The average fractions of energy are 0.56 in products relative translation, 0.28 in ONH_2 vibration, 0.13 in ONH_2 rotation, 0.00 in NH_2 vibration, and 0.03 in NH_2 rotation. Much as in the rest of channels examined in this work, most of the energy appears as products translation. The rest of energy goes to primarily into the molecule that carries the oxygen radical, which results vibrationally excited. In fact, over 30 kcal/mol above the zero-point level are channeled into ONH_2 vibration. Very little energy is deposited in the NH_2 fragment, which molecular modes seem to be orthogonal to the reaction coordinate.

D. Angular Distributions. We now describe the angular distributions calculated for all of the pathways of the $O + NH_3$ and $O + N_2H_4$ systems to further understand the reactions dynamics and mechanism. Figure 6 shows the angular distributions in the $O + NH_3$ (part a of Figure 6) and $O + N_2H_4$ (part b of Figure 6) abstraction and H-elimination reactions at $E_{coll} = 4.56$ eV. The angular distributions are presented in terms of normalized differential cross sections (DCS) as a function of the cosine of the angle formed between the reagents and products relative velocity vectors (**k** and **k'**, respectively).

Regarding the hydrogen-abstraction reactions, we see that the angular distributions span a wide range of scattering angles but are predominately forward. Analysis of the angular distributions at the lower collision energies calculated in this work (not shown) indicates that, in both the $O + NH_3$ and the $O + N_2H_4$ reactions, the angular distributions are essentially independent of collision energy. These results, taken together with the opacity functions in Figure 5 and the product energy partitioning analysis presented before, can be used to decipher the reaction mecha-

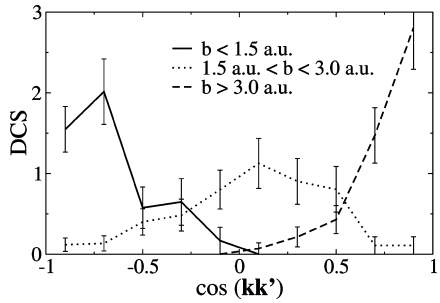

Figure 7. Angular distributions (normalized differential cross sections DCS vs the cosine of the scattering angle) for various ranges of the impact parameter (b) in the $O + N_2H_4 \rightarrow OH + N_2H_3$ reaction at $E_{coll} = 4.56$ eV.

nism. Forward scattering, together with reaction at long impact parameters and a large energy release into products translation, constitutes a rubric of stripping dynamics. In the stripping-dynamics mechanism, the hydrogen-abstraction reaction is direct and peripheral. Under those conditions, the incoming radical barely changes its momentum as it abstracts a hydrogen atom, and the newly formed diatomic product therefore scatters in the forward direction. Even though the main mechanism governing the hydrogen abstraction reaction appears to be stripping, the fact that the angular distribution spans a wide range of scattering angles, in addition to the possibility for reaction at low-impact parameter shown in the opacity functions of Figure 5, points to the contribution of other direct mechanisms. In these other direct mechanisms, reaction at low-impact parameters gives rise to sideways and backward scattering, as has been recently described in other gas-phase polyatomic reactions.[25] Further insight into the dependence of the scattering angle with the impact parameter for the hydrogen-abstraction channel can be gained from Figure 7, where we have plotted the angular distribution for trajectories scattered in various ranges of the impact parameter for the $O + N_2H_4 \rightarrow OH + N_2H_3$ reaction at $E_{coll} = 4.56$ eV. Clearly, reactions at low impact parameters ($b < 1.5$ au) all scatter in the backward hemisphere. On the other hand, high-impact-parameter reactions ($b > 3.0$ au) lead exclusively to scattering in the forward hemisphere. Reaction at intermediate parameters leads to more sideways scattering.

The H-elimination reaction shows markedly different angular distributions when compared to the hydrogen-abstraction reaction. Most of the trajectories leading to H-elimination exhibit strongly backward scattering, with the H radical traveling in the direction of approach of the striking O atoms (i.e., the oxyaminyl product recoils backward). When taken together with the opacity functions for this channel in Figure 5, which show a clear preference for reaction at low impact parameters, the angular distributions provide a solid indication of rebound dynamics. In rebound dynamics, a low-impact-parameter collision between the reagent species results in a hard hit that causes forward ejection of the light H atom and backward scattering of the O-containing coproduct. At the same time, the hard hit favors internal excitation of the newly formed polyatomic species as a consequence of the direct O−N interaction.

Comparison between the angular distributions for the abstraction and H-elimination channels in the $O + NH_3$ (part a of Figure 6) and $O + N_2H_4$ (part b of Figure 6) reactions shows that, in the reactions with the larger molecule, the tendency for forward and backward scattering in the abstraction and H-elimination channels respectively is exacerbated when compared with the $O + NH_3$ channels. Likely, the steric requirements imposed by the larger reagent molecule have a greater influence on the recoil directions of the product species than is the case with the smaller NH_3 reagent.

Although the low number of reactive $O + N_2H_4 \rightarrow ONH_2 + NH_2$ trajectories (15 out of 1000 calculated) does not permit us to obtain a smooth angular distribution, most of the trajectories in this channel exhibit strongly backward scattering. Visual analysis of these trajectories shows dynamics consistent with the saddle point and minimum-energy reaction path shown in Figures 1 and 3. In effect, reaction occurs in low-impact-parameter collisions that explore geometries in which the forming O−N bond is nearly parallel to the breaking N−N bond. This leads to the NH_2 fragment traveling in the direction of the incident O atom with little internal excitation and the ONH_2 radical recoiling backward with relatively high vibrational excitation.

Conclusions

We have investigated the reactions between ground-state oxygen atoms and the NH_3 and N_2H_4 molecules at hyperthermal energies using two techniques of the chemical-reaction theory.

First, we have carried out electronic-structure calculations to accurately characterize the stationary points in the potential-energy surface of the main reaction channels open at hyperthermal energies (<5 eV). Hydrogen abstraction producing OH and aminyl radicals is the lowest-barrier channel in both the $O + NH_3$ and N_2H_4 systems, requiring an energy of less than 0.5 eV for reaction. H-elimination reactions that produce H and oxyaminyl radicals exhibit a substantially larger barrier, in excess of 2 eV, and are strongly endothermic. An additional reaction pathway, N−N breakage to yield $ONH_2 + NH_2$ products, is possible in the $O+N_2H_4$ reaction. This channel is notably exothermic and proceeds through a barrier with a height intermediate between that of hydrogen abstraction and H-elimination. A comparison between the common reaction pathways in $O + NH_3$ and N_2H_4 reactions reveals that the hydrazine reactions are more exothermic and possess smaller barriers than the reactions with ammonia. An essential result of the comparison of the performance of various electronic-structure methods is that the relatively low cost BHandHLYP/6-31G* level reproduces remarkably well higher-accuracy CCSD(T) calculations in all of the reaction channels explored in this work. This result has enabled us to investigate the reactions dynamics with some confidence of accuracy by propagating quasiclassical trajectories directly with this DFT method.

The reaction-dynamics calculations indicate that hydrogen abstraction is the dominant reaction channel even at energies well above the barriers of the rest of reaction channels. However, whereas the cross section for the H-elimination reaction becomes within a factor of 2 of the abstraction cross section in $O + NH_3$ at $E_{coll} = 4.56$ eV, both the H-elimination and the N−N breakage cross sections are more than 1 order of magnitude smaller than those for hydrogen abstraction in $O + N_2H_4$ at all collision energies. Analysis of energy partitioning in products for the hydrogen-abstraction reactions indicates that most of the relative initial translational energy is retained as products relative translation. This is particularly true for the $O + NH_3 \rightarrow OH + NH_2$ reaction, where less than 25% of the available energy ends up in molecular modes. Slightly more energy is channeled into internal modes of the recoiling molecules in the $O + N_2H_4 \rightarrow OH + N_2H_3$ reaction, which we attribute to the better coupling of molecular modes to the reaction coordinate in this larger reaction. For instance, the amount of energy channeled into the

OH product in O + N_2H_4 collisions is large enough that about 50% of the trajectories lead to vibrationally excited OH at the energies examined in this work. In the rest of reaction pathways, the available energy is also primarily diverted into products relative translation. However, even if relative translation is the preferred mode for energy deposition in products, the large amount of available energy makes it possible for oxyaminyl fragments (ONH_2, ON_2H_3) to emerge with substantial vibrational excitation.

Finally, examination of the calculated angular distributions and opacity functions enables us to ascertain the mechanism of the various reaction pathways. Hydrogen abstraction occurs through a wide range of impact parameters and yields products that scatter in multiple directions. However, the peak of the angular distributions is clearly in the forward direction, and analysis of the scattering angle as a function of the impact parameter provides evidence that a large fraction of the collisions leading to hydrogen abstraction undergo a stripping mechanism. These results are in sharp contrast with those emerging from the H-elimination reaction channel. This channel combines reactions at low-impact parameters with strongly backward angular distributions, which are signatures of a direct rebound mechanism. The dynamics properties of the N−N breakage channel resemble those of the H-elimination channel.

Acknowledgment. This work has been funded by AFOSR Grant No. FA9550-09-0184 and by NSF (CHE-0547543). D.T. is a Cottrell Scholar of the Research Corporation for Science Advancement.

References and Notes

(1) Leger, L. J.; Visentine, J. T. *J. Spacecr. Rockets* **1986**, *23* (5), 505–511.

(2) Murr, L. E.; Kinard, W. H. *Am. Scientist* **1993**, *81* (2), 152–165.

(3) Roble, R. G. Energetics of the mesosphere and thermosphere. In *The Upper Mesosphere and Lower Thermosphere: A Review of Experiment and Theory (Geophysical Monograph)*; Johnson, R. M., Killeen, T. L.,Eds. 1995; Vol. 87, p 1.

(4) Minton, T. K.; Garton, D. J., Dynamics of atomic-oxygen-induced polymer degradation in low earth orbit. In *Advanced Series in Physical Chemistry (Chemical Dynamics in Extreme Environments)*; 2001; Vol. 11.

(5) Troya, D.; Schatz, G. C. *Int. Rev. Phys. Chem.* **2004**, *23* (3), 341–373.

(6) Garton, D. J.; Minton, T. K.; Troya, D.; Pascual, R.; Schatz, G. C. *J. Phys. Chem. A* **2003**, *107* (23), 4583–4587.

(7) Simmons, F. S. *Rocket Exhaust Plume Phenomenology*; The Aerospace Press: El Segundo, CA, 2000.

(8) Bernstein, L. S.; Chin, Y. H.; Gardner, J. A.; Broadfoot, A. L.; Lester, M. I.; Tsiouris, M.; Dressler, R. A.; Murad, E. *J. Phys. Chem. A* **2003**, *107* (49), 10695–10705.

(9) Bernstein, L. S.; Braunstein, M.; Broadfoot, A. L.; Dimpfl, W. L.; Dressler, R. A.; Chiu, Y. H.; Gardner, J. A.; Murad, E. *J. Spacecr. Rockets* **2006**, *43* (6), 1370–1376.

(10) Hester, B. D.; Chiu, Y. H.; Winick, J. R.; Dressler, R. A.; Bernstein, L. S.; Braunstein, M.; Sydney, P. F. *J. Spacecr. Rockets* **2009**, *46* (3), 679–688.

(11) http://www.defenselink.mil/releases/release.aspx?releaseid=11704.

(12) Espinosa-Garcia, J. *J. Phys. Chem. A* **2000**, *104* (32), 7537–7544.

(13) Cohen, N. *Int. J. Chem. Kinet.* **1987**, *19* (4), 319–362.

(14) Lang, V. L. *J. Phys. Chem.* **1992**, *96*, 3047–3050.

(15) Vaghjiani, G. L. *J. Chem. Phys.* **1996**, *104* (14), 5479–5489.

(16) Vaghjiani, G. L. *J. Phys. Chem. A* **2001**, *105* (19), 4682–4690.

(17) Orient, O. J.; Chutjian, A.; Murad, E. *J. Chem. Phys.* **1994**, *101* (10), 8297–8301.

(18) Frisch, M. J. Trucks, G. W.; Schlegel, H. B.; Scuseria, G. E.; Robb, M. A.; Cheeseman, J. R.; Montgomery, J., J. A.; Vreven, T.; Kudin, K. N.; Burant, J. C.; Millam, J. M.; Iyengar, S. S.; Tomasi, J.; Barone, V.; Mennucci, B.; Cossi, M.; Scalmani, G.; Rega, N.; Petersson, G. A.; Nakatsuji, H.; Hada, M.; Ehara, M.; Toyota, K.; Fukuda, R.; Hasegawa, J.; Ishida, M.; Nakajima, T.; Honda, Y.; Kitao, O.; Nakai, H.; Klene, M.; Li, X.; Knox, J. E.; Hratchian, H. P.; Cross, J. B.; Bakken, V.; Adamo, C.; Jaramillo, J.; Gomperts, R.; Stratmann, R. E.; Yazyev, O.; Austin, A. J.; Cammi, R.; Pomelli, C.; Ochterski, J. W.; Ayala, P. Y.; Morokuma, K.; Voth, G. A.; Salvador, P.; Dannenberg, J. J.; Zakrzewski, V. G.; Dapprich, S.; Daniels, A. D.; Strain, M. C.; Farkas, O.; Malick, D. K.; Rabuck, A. D.; Raghavachari, K.; Foresman, J. B.; Ortiz, J. V.; Cui, Q.; Baboul, A. G.; Clifford, S.; Cioslowski, J.; Stefanov, B. B.; Liu, G.; Liashenko, A.; Piskorz, P.; Komaromi, I.; Martin, R. L.; Fox, D. J.; Keith, T.; Al-Laham, M. A.; Peng, C. Y.; Nanayakkara, A.; Challacombe, M.; Gill, P. M. W.; Johnson, B.; Chen, W.; Wong, M. W.; Gonzalez, C.; Pople, J. A. *GAUSSIAN 03*, Rev. C.02; Gaussian, Inc.: Wallingford, CT, 2004.

(19) Reaction energies calculated from the experimental heats of formation at 298 K reported in http://webbook.nist.gov/chemistry.

(20) Layfield, J. P.; Owens, M. D.; Troya, D. *J. Chem. Phys*. **2008**, *128* (19).

(21) Troya, D. *J. Phys. Chem. A* **2007**, *111* (42), 10745.

(22) Hammond, G. S. *J. Am. Chem. Soc.* **1955**, *77* (2), 334–338.

(23) Zhang, J. M.; Camden, J. P.; Brunsvold, A. L.; Upadhyaya, H. P.; Minton, T. K.; Schatz, G. C. *J. Am. Chem. Soc.* **2008**, *130* (28), 8896.

(24) Levine, R. D. *Molecular Reaction Dynamics*; Cambridge University Press: Cambridge, UK, New York, 2005.

(25) Camden, J. P.; Hu, W. F.; Bechtel, H. A.; Brown, D. J. A.; Martin, M. R.; Zare, R. N.; Lendvay, G.; Troya, D.; Schatz, G. C. *J. Phys. Chem. A* **2006**, *110* (2), 677–686.

JP9072747